Chinese Chemical Letters 35 (2024) 109388

Contents lists available at ScienceDirect

Chinese Chemical Letters

journal homepage: www.elsevier.com/locate/cclet

Ni_xB/rGO as the cathode for high-performance aqueous alkaline zinc-based battery

Xiaoxing Ji[a,1], Xiaojuan Li[a,1], Chenggang Wang[a], Gang Zhao[a], Hongxia Bu[b,*], Xijin Xu[a,*]

[a] School of Physics and Technology, University of Jinan, Ji'nan 250022, China
[b] College of Physics and Electronic Engineering, Qilu Normal University, Ji'nan 250200, China

ARTICLE INFO

Article history:
Received 31 October 2023
Revised 27 November 2023
Accepted 6 December 2023
Available online 14 December 2023

Keywords:
Alkaline aqueous zinc battery
Nickel boride
rGO
Cathode materials
Energy density

ABSTRACT

Aqueous alkaline zinc batteries (AZBs) exhibit great potential due to their high capacity, high safety and low cost. However, despite these advantages, the lack of high stability and high utilization rate makes the search for high-performance cathode materials a great challenge. Here, an amorphous nickel boride/rGO (Ni_xB/rGO) complex structure was designed. As a result of abundant unsaturated active sites and synergistic electronic effects, amorphous Ni_xB exhibits excellent energy storage properties. As well as having high electrical conductivity, rGO avoids aggregation of Ni_xB nanoparticles, ensuring that Ni_xB/rGO electrodes have a high energy storage capacity. The structure has a strong adhesion between Ni_xB and rGO, which protects its stable structure and extends its life. More importantly, the Ni_xB/rGO//Zn full battery shows remarkable capacity (228.4 mAh/g at 2 A/g), extraordinary cycle durability (93.7% retained after 1000 cycles) and strong energy density 399.7 Wh/kg, when coupled with Ni_xB/rGO cathode. This work will also shed light on other nickel-zinc batteries in order to achieve super durability and capacity.

The rapidly increasing demand for energy and global environmental degradation has prompted researchers to seek alternative green energy sources, putting further demands on energy storage devices [1–5]. While lithium-ion batteries remain dominant in commercial energy storage markets, their toxic explosive electrolytes and scarce lithium-metal sources are not sustainable [6–8]. So researchers have turned to high-safe, low-cost aqueous rechargeable batteries. Zinc-based batteries using zinc metal have garnered significant attention due to their natural benefits such as abundant sources and high theoretical specific capacity (820 mAh/g or 5855 mAh/cm^3) [9–11]. Furthermore, the Zn^{2+}/Zn reversible redox reactions take place in an alkaline electrolyte with a much lower potential (−1.26 V *vs.* SHE) compared to a near-neutral or mildly acidic electrolyte (−0.76 V *vs.* SHE) [10,12–14]. However, the current lack of high-performance positive electrodes with high rate and stability severely restricts the application of aqueous alkaline zinc batteries (AZBs) [15–17].

In the past studies on AZBs cathodes mainly focused on transition metal oxides and hydroxides, including MnO_2 [18], nickel/cobalt oxides/hydroxides [19], vanadium-based oxides [20]. However, the predominant problems associated with alkaline Zn/MnO_2 batteries include low output voltage and poor cycling stability [21]. In spite of high working voltage (1.8 V) and theoretical energy density (372 Wh/kg), its actual energy density is very low and its cycle life is unsatisfactory [22–24]. For this reason, nickel/cobalt-based materials were subjected to various modifications, such as vulcanization, carbonation, nitriding, phosphating [3,25,26]. Li *et al.* [27] successfully synthesized Ni_2P/C using glucose as carbon source under one-pot hydrothermal method and exhibited 176 mAh/g at 1 A/g. Yao *et al.* [28] prepared three-dimensional nitrogen-boron co-doped carbon quantum dots/reduced graphene oxide (N,B-CQDs/rGO) composite aerogels as zinc ion hybrid capacitors and the N,B-CQDs/rGO//Zn hybrid capacitor exhibited a high energy density of 96.2 Wh/kg at 80 W/kg. Furthermore, transition metal borides exhibit excellent electrical conductivity, abundant reserves and green environment protection [29], showing broad prospects in electrochemistry [30] and energy storage [31]. Wang *et al.* [32] proposed that rGO/Co-B nanocomposite as an anode for lithium-ion storage exhibits a considerable reversible capacity of 894 mAh/g at 50 A/g. It is found that the introduced rGO interface is close to nanomaterials, which improves the conductivity and storage performance of cathode materials.

In this work, we have synthesized Ni_xB nanoparticles bonded to rGO, which serve as cathode material of AZBs. rGO improves electrical conductivity significantly, avoids the aggregation of Ni_xB nanoparticles, endows Ni_xB/rGO with high specific surface area and

* Corresponding authors.
E-mail addresses: buhx66@163.com (H. Bu), sps_xuxj@ujn.edu.cn (X. Xu).
[1] These authors contributed equally to this work.

https://doi.org/10.1016/j.cclet.2023.109388
1001-8417/

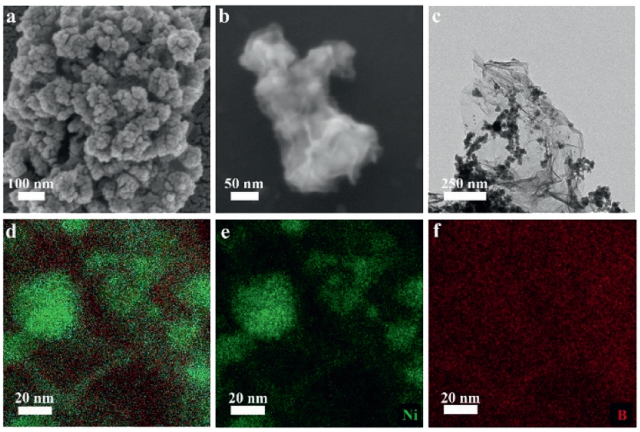

Fig. 1. SEM images of (a) Ni_xB, (b) Ni_xB/rGO. (c) TEM image of Ni_xB/rGO. (d-f) Mapping image of Ni_xB/rGO and Ni, B elements.

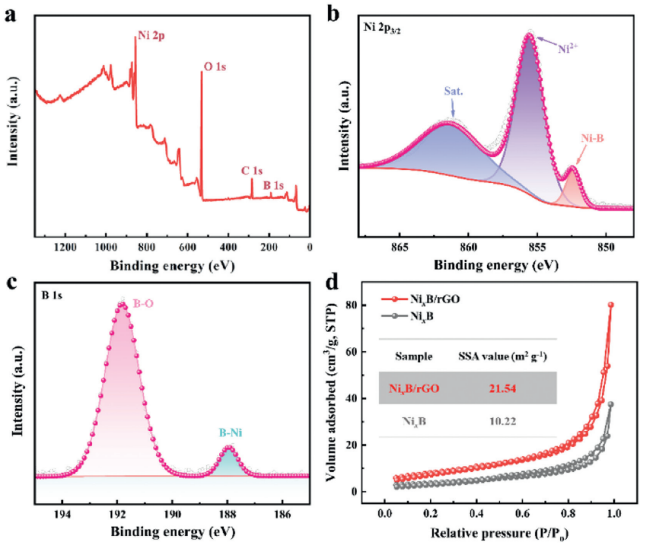

Fig. 2. (a) XPS survey spectrum. XPS spectra of (b) Ni $2p_{3/2}$ and (c) B 1s. (d) Plots of N_2 adsorption-desorption isotherm and pore size distribution of Ni_xB and Ni_xB/rGO.

high capacity. The specific capacity of Ni_xB/rGO composite cathode material reaches 241.9 mAh/g at 2 A/g. The Ni_xB/rGO//Zn battery, as prepared, shows strong power density at 34 kW/kg, and ultra-high energy density at 399.7 Wh/kg.

Ni_xB is a type of nanoparticles with an approximately 30 nm particle size (Fig. 1a) and this extra-fine particle size helps to reduce the diffusion distance of the ions and improve the reaction kinetics. The diffraction pattern of Ni_xB (Fig. S1a in Supporting information) shows its amorphous structure. In Fig. S1b (Supporting information), there is no apparent lattice spacing for Ni_xB HRTEM, which further illustrates the amorphous feature. The SEM image of Ni_xB/rGO in Fig. 1b reveals that the Ni_xB is tightly wrapped by the rGO. The rGO is served as the expressway for charge transfer owing to the high conductivity of rGO. The TEM image of Ni_xB/rGO in Fig. 1c shows that Ni_xB nanoparticles dispersed uniformly on rGO with smaller sizes, which greatly increased the specific area and active sites. In Figs. 1d–f, elemental maps show that Ni and B dispersion are uniformly distributed. The Ni_xB nanoparticles are distributed uniformly on rGO surface.

The XRD patterns of Ni_xB and Ni_xB/rGO (Fig. S2 in Supporting information) show broad peaks at 45°, confirming its amorphous characteristic. The small peaks located at around 34° and 60° are ascribed to the HBO_2, which are formed when the reaction is carried out in aqueous solution [35]. As a control group, we have pyrolyzed Ni_xB to synthesize crystalline Ni_xB (denoted as Ni_xB-400). In the XRD pattern (Fig. S3 in Supporting information) of Ni_xB-400, weak diffraction peaks at 34.4°, 37.1° and 62.5° are assigned to the (200) (210) and (141) plane of the Ni_3B (JCPDS card No. 48–1223) phase, respectively. Further investigation was carried out on Ni_xB/rGO components and valence states, as illustrated in Figs. 2a–c, by XPS. The entire XPS spectrum (Fig. 2a) clearly shows peak values for Ni 2p, O 1s and B 1s. The Ni $2p_{3/2}$ spectrum of Ni_xB in Fig. 2b shows binding energies at 855.6 eV designated as oxidized material (Ni^{2+}) [33,34]. It can be attributed to the compound action of rGO and Ni_xB nanoparticles. The lower binding energy at 852.4 eV is conformable to Ni-B bonds, and the peak at 862 eV is attributed to a satellite peak (denoted as "Sat.") [35]. At 187.9 eV and 191.7 eV in B 1s spectrum (Fig. 2c) belong to element B (B^0) and oxidation state (BO_2^-), respectively [36,37]. The oxidation state peak is caused by rGO. Based on these results, the shell should contain $Ni(BO_2)_2$ while the core consists of Ni_xB. In the BO_2^- group, the number of valence electrons of B is 3, and the total number of electrons is 6, indicating that B is in an electron-deficient state [35]. In this case, the $Ni(BO_2)_2$ layer enhances the adsorption of OH^- ions and improves the reaction kinetics. Furthermore, the specific surface area of Ni_xB/rGO (21.54 m^2/g) is much larger than Ni_xB (10.22 m^2/g) in the assessment of nitrogen adsorption/desorption test shown in Fig. 2d. This suggests that the addition of rGO can improve the dispersion of Ni_xB in the nanoparticles.

The electrochemical properties of Ni_xB, Ni_xB/rGO and Ni_xB-400 electrodes have been tested in 3 mol/L potassium hydroxide with a three-electrode system. The CV curves of Ni_xB, Ni_xB/rGO and Ni_xB-400 electrodes show two strong oxidation–reduction peaks at 10 mV/s scanning rate (Fig. 3a). The larger closed area of Ni_xB/rGO indicates higher specific capacity [38]. The GCD contrast curve in Fig. 3b shows that the specific capacity of the Ni_xB/rGO electrode (241.9 mAh/g) at 2 A/g is much higher than pure Ni_xB and crystal Ni_xB-400 [39]. Correspondingly, as shown in Fig. S4 (Supporting information), Ni_xB/rGO electrode has an area capacity of 1.69 mAh/cm^2, which is higher than 2 mA/cm^2 for Ni_xB electrode and 1.24 mAh/cm^2. The CV curves of the Ni_xB and Ni_xB/rGO electrodes at different scan rates are shown in Fig. 3c and Fig. S5 (Supporting information), where the redox peaks shifted along the opposite positive and negative directions when the scan rate was increased from 2 mV/s to 15 mV/s, which stemmed from the internal resistance of the electrodes and the polarization induced by the high scan rate. In Fig. 3d, the charge and discharge characteristics of Ni_xB/rGO electrodes from 2 A/g to 30 A/g current density are described. The results show that Ni_xB/rGO electrode has symmetrical charge-discharge curves with high efficiency. At current densities 2, 5, 8, 10, 15, 20, 30 A/g, Ni_xB/rGO electrodes exhibit capacities of 241.9, 231.1, 221.5, 215.0, 202.5, 188.7 and 163.4 mAh/g respectively (Fig. 3e). As shown in Figs. S6 and S7 (Supporting information), Ni_xB/rGO electrodes also have excellent area-specific capacity. Besides, the linear fit results of relationship between log peak current and log scan rate for Ni_xB and Ni_xB/rGO electrodes were recorded in Figs. S8 and S9 (Supporting information). The b values of Ni_xB and Ni_xB/rGO were calculated based on the equation:

$$i = av^b \tag{1}$$

where v represents the scan rate and i represents the response current. The b values were fitted as 0.56/0.62 (b_1/b_1') for Ni_xB and 0.66/0.59 (b_2/b_2') for Ni_xB/rGO, implying that the reaction is diffusion-controlled. Although it is diffusion-controlled, the Ni_xB/rGO has superior reaction kinetics. It is further proved by the rate performance in Fig. 3e, demonstrating that the Ni_xB/rGO is a new kind of high-rate cathode material.

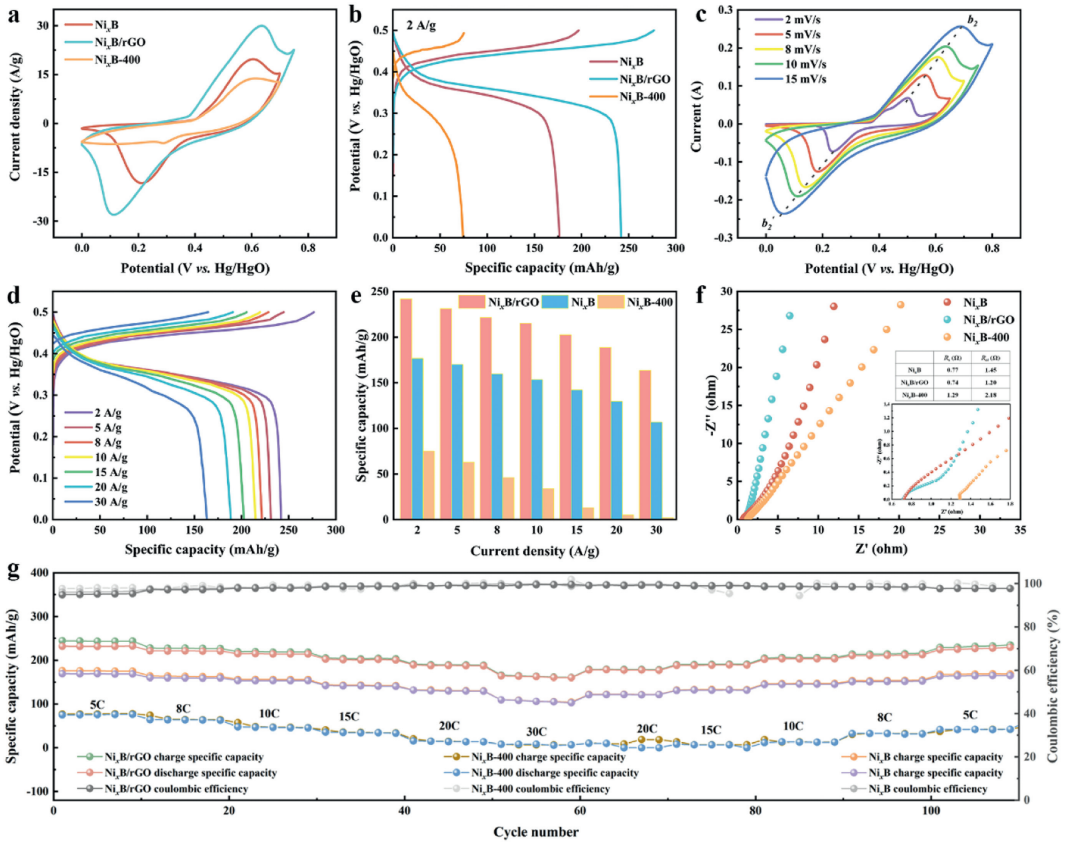

Fig. 3. (a) CV curves of Ni$_x$B, Ni$_x$B/rGO and Ni$_x$B-400 electrodes with a scan rate of 10 mV/s. (b) GCD curves of Ni$_x$B, Ni$_x$B/rGO and Ni$_x$B-400 electrodes under a current density of 2 A/g. (c) CV curves of Ni$_x$B/rGO electrodes under various scan rates. (d) GCD curves of Ni$_x$B/rGO electrodes at different current densities. (e) Mass specific capacities of Ni$_x$B, Ni$_x$B/rGO and Ni$_x$B-400 electrodes. (f) EIS profiles of the Ni$_x$B, Ni$_x$B/rGO and Ni$_x$B-400 electrodes. (g) Rate performance of the Ni$_x$B, Ni$_x$B/rGO and Ni$_x$B-400 electrodes.

To illustrate the reaction kinetics, the EIS measurements are shown in Fig. 3f, where the measured impedance data consists of equivalent series resistance (R_s), charge transfer resistance (R_{ct}) and constant phase element (CPE) (Fig. S10 in Supporting information). The impedance spectra in the high-frequency region show that Ni$_x$B/rGO electrode has a lower charge transfer resistance ($R_{ct} = 1.20\ \Omega$), which indicates the high charge transfer capability of the Ni$_x$B/rGO electrode. This is mainly due to the abundant active sites of the amorphous material.

Fig. 3g displays the discharge characteristics of Ni$_x$B and Ni$_x$B/rGO electrodes, which retain 70% and 64% of their original capacity at a high current density (30 A/g), respectively. In contrast the crystal Ni$_x$B-400 has poor multiplicative properties. The Ni$_x$B/rGO electrode exhibits better high-quality specific and high area-specific capacity, indicating that the addition of rGO increases the active reaction site and accelerates the charge transfer while improving the capacity and rate performance of the Ni$_x$B/rGO electrode.

To further demonstrate the suitability of the Ni$_x$B/rGO cathode in AZBs, 1% $Zn(OAc)_2$ solution was added to 3 mol/L potassium hydroxide as electrolyte, zinc foil was used as anode (Fig. 4a). The reaction mechanism of Ni$_x$B/rGO//Zn cell is summarized in the following equation:

Cathode reaction:

$$2Ni_xB + (4x+6)OH^- \rightarrow (2x-3)Ni(OH)_2 + Ni_3(BO_3)_2 + 6H_2O + (4x+6)e^- \quad (2)$$

$$Ni(OH)_2 + OH^- \rightleftharpoons NiOOH + H_2O + e^- \quad (3)$$

Anode reaction:

$$[Zn(OH_4)]^{2-} + 2e^- \rightleftharpoons Zn + 4OH^- \quad (4)$$

Overall:

$$4Ni_xB + (6x+3)[Zn(OH_4)]^{2-} \rightleftharpoons (4x-6)NiOOH + 2Ni_3(BO_3)_2 + (6x+3)Zn + (12x+6)OH^- + (4x+6)H_2O \quad (5)$$

The CV curve of Ni$_x$B/rGO//Zn battery is shown in Fig. 4b at 1.4–2.2 V. With the scan rates increasing, the CV shapes slightly change, indicating the fast reaction kinetics and high redox reaction reversibility. In Fig. 4c, the GCD curves indicate that Ni$_x$B/rGO//Zn batteries show good discharge capacity (228.4 mA/g) at 2 A/g. At 2, 5, 8, 10, 15 and 20 A/g the capacity of Ni$_x$B/rGO//Zn batteries is 228.4, 224.0, 214.1, 204.7, 181.2 and 148.3 mAh/g, respectively. In Fig. 4d, the Ni$_x$B/rGO//Zn battery is still present at 65% of its original capacity at 20 A/g. In Fig. 4e, the maximum discharge capacity of the Ni$_x$B/rGO//Zn battery can reach 228.4 mAh/g at 2 C. Even at a high current density of 30 C, Ni$_x$B/rGO//Zn battery still maintains a high discharge specific capacity of 98.4 mAh/g, which indicates its excellent rate performance. The Ni$_x$B/rGO//Zn battery maintains 93.7% of the first lap capacity after 1000 cycles under 10 A/g high current density, as shown in Fig. 4f. To demonstrate the outstanding advantages of our designed Ni//zinc battery, we compare with other reported water-based storage devices in terms of optimal performance. The maximum energy density of Ni$_x$B/rGO//Zn batteries is 399.7 Wh/kg at 3.5 kW/kg as shown in the Ragone diagram in Fig. 4g. Furthermore, the energy density of the Ni$_x$B/rGO//Zn battery remains at 252.11 Wh/kg when the power density is 34 kW/kg, exceeding that of many recently reported other energy storage devices [21,40–44]. Moreover, we make comparisons of the cathode

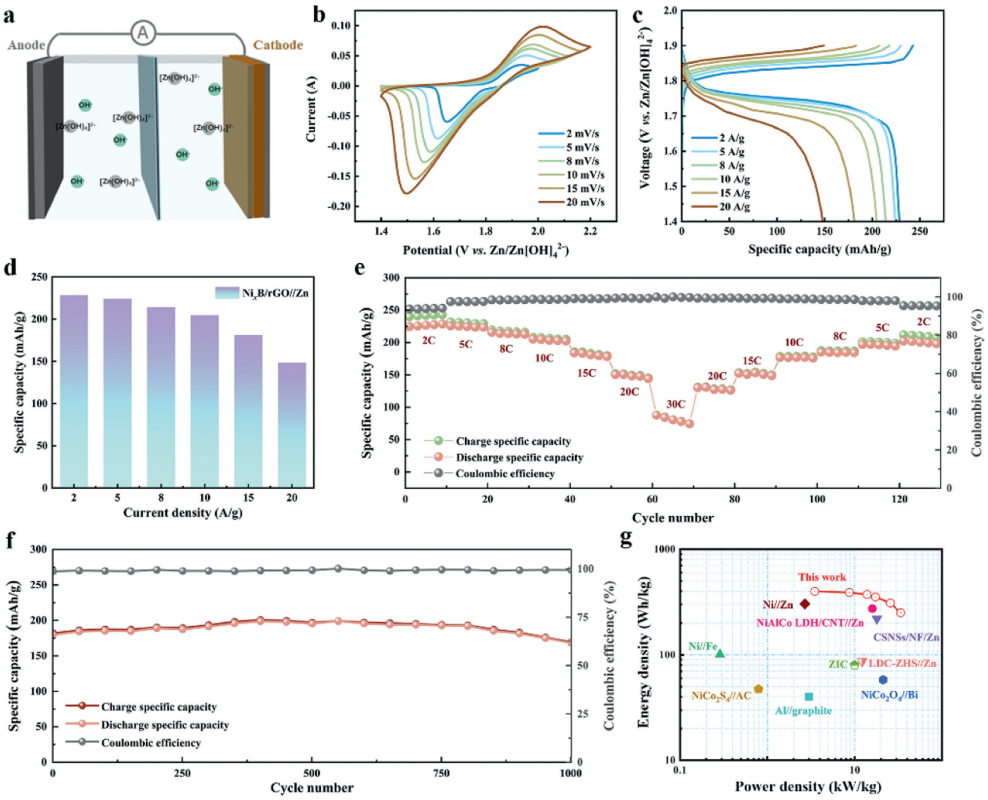

Fig. 4. (a) Schematic diagram of Ni$_x$B/rGO//Zn battery. (b) CV curves of the Ni$_x$B/rGO//Zn battery at various scan rates. (c) Charge and discharge profiles of the Ni$_x$B/rGO//Zn battery under different current densities. (d) Specific capacity of Ni$_x$B/rGO//Zn battery at different current densities. (e) Rate performance of the as-assembled Ni$_x$B/rGO//Zn battery. (f) Cycling performance of Ni$_x$B/rGO//Zn battery. (g) Ragone plots of the Ni$_x$B/rGO//Zn battery. The values reported for other aqueous batteries are added for comparison.

capacity of Ni$_x$B/rGO//Zn battery with other alkaline zinc-based batteries. The Ragone plot in Fig. S11 (Supporting information) shows that the capacity of Ni$_x$B/rGO//Zn is superior to many previous reports on alkaline zinc-based batteries such as $NiCo_2O_4$//Zn, NiAlCo LDH/CNT//Zn.

In summary, it is concluded that Ni$_x$B nanoparticles attached to rGO have been synthesized by chemical precipitation method and treated as cathode of alkaline nickel-zinc battery. Addition of rGO can improve the electron transfer rate and conductivity of Ni$_x$B/rGO electrode greatly improve its specific capacity and cycle stability. Furthermore, the assembled Ni$_x$B/rGO//Zn batteries show high energy density at 399.7 Wh/kg (3.5 kW/kg power density) and long cycle life (93.7% of initial capacity after 1000 cycles at 10 A/g). To sum up, Ni$_x$B/rGO electrodes are excellent cathode materials for nickel-zinc batteries. The assembled AZBs are highly secure, robust, and have high potential for application.

Declaration of competing interest

The authors declare that they have no known competing financial interests or personal relationships that could have appeared to influence the work reported in this paper.

Acknowledgments

This work was supported by Joint Funds of the National Natural Science Foundation of China (No. U22A20140), the Natural Science Foundation of Shandong Province, China (No. ZR2021MA073). All the authors discussed the results and commented on the manuscript. The authors would like to thank the Shiyanjia Lab (www.shiyanjia.com) for the support of TEM and XPS tests.

Supplementary materials

Supplementary material associated with this article can be found, in the online version, at doi:10.1016/j.cclet.2023.109388.

References

[1] C. Wang, S. Zhao, X. Song, et al., Adv. Energy Mater. 12 (2022) 2200157.
[2] S. Zhao, C. Li, X. Zhang, et al., Sci. Bull. 68 (2023) 56–64.
[3] X. Zhang, G. Qu, Z. Wang, et al., Chin. Chem. Lett. 32 (2021) 2453–2458.
[4] Q. Li, K. Ma, C. Hong, et al., Sci. China Mater. 64 (2021) 1386–1395.
[5] J. Jiang, J. Liu, Interdiscip. Mater. 1 (2022) 116–139.
[6] W. Qiao, B. Jin, W. Xie, et al., J. Energy Chem. 69 (2022) 9–15.
[7] X. Wang, Z. Gu, E.H. Ang, et al., Interdiscip. Mater. 1 (2022) 417–433.
[8] Y. Shi, Y. Chen, L. Shi, et al., Small 16 (2020) 2000730.
[9] M. Zhu, Nano Res. Energy 2 (2023) e9120038.
[10] W. Shang, W. Yu, Y. Liu, et al., Energy Stor. Mater. 31 (2020) 44–57.
[11] H. Ge, X. Feng, D. Liu, et al., Nano Res. Energy 2 (2023) e9120039.
[12] Y. Wang, Q. Li, H. Hong, et al., Nat. Commun. 14 (2023) 3890.
[13] C. Li, Q. Li, Z. Wu, et al., Adv. Mater. (2023) 2304878.
[14] S. Chai, J. Xia, Y. Li, et al., Energy (2023) 100077.
[15] C. Li, S. Zhao, X. Zhang, et al., Chem. Eng. J. 450 (2022) 137998.
[16] N. Li, G. Qu, X. Zhang, et al., Chin. Chem. Lett. 33 (2022) 3272–3276.
[17] X. Li, T. Wang, C. Li, et al., Chem. Eng. J. 451 (2023) 138526.
[18] H. Tang, W. Chen, N. Li, et al., Energy Stor. Mater. 48 (2022) 335–343.
[19] H. Zhang, R. Wang, D. Lin, et al., ChemNanoMat 4 (2018) 525–536.
[20] D. Zhao, X. Wang, W. Zhang, et al., Adv. Funct. Mater. 33 (2023) 2211412.
[21] M. Huang, M. Li, C. Niu, et al., Adv. Funct. Mater. 29 (2019) 1807847.
[22] D. Chao, W. Zhou, F. Xie, et al., Sci. Adv. 6 (2020) eaba4098.
[23] M. Gong, Y. Li, H. Zhang, et al., Energy Environ. Sci. 7 (2014) 2025–2032.
[24] H. Li, L. Ma, C. Han, et al., Nano Energy 62 (2019) 550–587.
[25] B. Liu, X. Liu, X. Fan, et al., J. Alloys Compd. 834 (2020) 155185.
[26] X. Li, S. Zhao, G. Qu, et al., J. Mater. Sci. Technol. 118 (2022) 190–198.
[27] J. Li, C. Chen, Mater. Res. Express 5 (2018) 015502.
[28] J.J. Yao, C. Liu, J.Y. Li, et al., Rare Metals 42 (2023) 2307–2323.
[29] E. Ozdemir, Int. J. Hydrog. Energy 40 (2015) 14045–14051.
[30] S. Gupta, N. Patel, A. Miotello, et al., J. Power Sources 279 (2015) 620–625.
[31] S. Qiu, J. Huang, F. Shen, et al., Int. J. Hydrog. Energy 41 (2016) 3955–3960.
[32] D. Wang, J. Zhou, J. Li, et al., Chem. Eng. J. 360 (2019) 271–279.
[33] H. Chen, J. Jiang, Y. Zhao, et al., J. Mater. Chem. A 3 (2015) 428–437.

[34] T. Chen, F. Deng, J. Zhu, et al., J. Med. Chem. 22 (2012) 15190–15197.
[35] Y. Chen, T. Zhou, L. Li, et al., ACS Nano 13 (2019) 9376–9385.
[36] G.M. Arzac, T.C. Rojas, A. Fernandez, et al., ChemCatChem 3 (2011) 1305–1313.
[37] Y. Kang, B. Jiang, J. Yang, et al., ACS Nano 14 (2020) 17224–17232.
[38] X. Feng, Y. Huang, C. Li, et al., Chem. Eng. J. 368 (2019) 51–60.
[39] S. Carenco, D. Portehault, C. Boissiere, et al., Chem. Rev. 113 (2013) 7981–8065.
[40] H. Zhang, X. Zhang, H. Li, et al., Green Energy Environ. 3 (2018) 56–62.
[41] Y. Zeng, Z. Lin, Y. Meng, et al., Adv. Mater. 28 (2016) 9188–9195.
[42] M.C. Lin, M. Gong, B. Lu, et al., Nature 520 (2015) 324–328.
[43] M. Shi, M. Zhao, L. Jiao, et al., J. Power Sources 509 (2021) 230333.
[44] Y. Shen, K. Zhang, F. Yang, et al., Sci. China Mater. 63 (2020) 1205–1215.